Reconstruction of sub-wavelength features and nano-positioning of gratings using coherent Fourier scatterometry

Nitish Kumar,[1,*] Peter Petrik,[1,2] Gopika K P Ramanandan,[1] Omar El Gawhary,[1,3] Sarathi Roy,[1] Silvania F Pereira,[1] Wim M J Coene,[4] and H. Paul Urbach[1]

[1]*Optics Research Group, Department of Imaging Physics, Faculty of Applied Sciences, Delft University of Technology, Van der Waalsweg 8, 2628CH Delft, The Netherlands*
[2]*Research Centre for Natural Sciences, Institute for Technical Physics and Materials Science, Hungarian Academy of Sciences, H-1121 Budapest, Konkoly Thege Miklós út 29-33, Hungary*
[3]*VSL Dutch Metrology Institute, Thijsseweg 11, 2600 AR Delft, The Netherlands*
[4]*ASML Netherlands B.V., De Run 6501, 5504 DR Veldhoven, The Netherlands*
[*]*N.Nitishkumar-1@tudelft.nl*

Abstract: Optical scatterometry is the state of art optical inspection technique for quality control in lithographic process. As such, any boost in its performance carries very relevant potential in semiconductor industry. Recently we have shown that coherent Fourier scatterometry (CFS) can lead to a notably improved sensitivity in the reconstruction of the geometry of printed gratings. In this work, we report on implementation of a CFS instrument, which confirms the predicted performances. The system, although currently operating at a relatively low numerical aperture (NA = 0.4) and long wavelength (633 nm) allows already the reconstruction of the grating parameters with nanometer accuracy, which is comparable to that of AFM and SEM measurements on the same sample, used as reference measurements. Additionally, 1 nm accuracy in lateral positioning has been demonstrated, corresponding to 0.08% of the pitch of the grating used in the actual experiment.

OCIS codes: (120.3940) Metrology; (290.5820) Scattering measurement; (180.5810) Scanning microscopy; (050.1950) Diffraction gratings.

References and links

1. "International technology roadmap for semiconductors," (2012). Available from http://www.itrs.net/Links/2012ITRS/2012Chapters/2012Overview.pdf.
2. C. Edwards, A. Arbabi, G. Popescu, and L. L. Goddard, "Optically monitoring and controlling nanoscale topography during semiconductor etching," Light: Sci. Appl. **1**, e30 (2012).
3. E. Vogel, "Technology and metrology of new electronic materials and devices," Nat. Nano. **2**(25), 25–32 (2007).
4. J. Lindberg, "Mathematical concepts of optical superresolution," J. Opt. **14**, (083001) (2012).
5. H. P. Baltes, ed., *Inverse Source Problems in Optics*, *Vol. 9 of Topics in Current Physics* (Springer-Verlag, 1978).
6. C. Raymond, "Overview of scatterometry applications in high volume silicon manufacturing," AIP Conf. Proc. **788**, 394–402 (2005).
7. H. T. Huang and F. L. Terry-Jr, "Erratum to spectroscopic ellipsometry and reflectometry from gratings (scatterometry) for critical dimension measurement and in situ, real-time process monitoring," Thin Solid Films **468**(1-2), 339–346 (2004).
8. Q. Zhan and J. R. Leger, "High-resolution imaging ellipsometer," App. Opt. **41**, 4443–4450 (2002).

#215012 - $15.00 USD Received 30 Jun 2014; revised 17 Aug 2014; accepted 19 Aug 2014; published 1 Oct 2014

9. P. Boher, J. Petit, T. Leroux, J. Foucher, Y. Desieres, J. Hazart, and P. Chaton, "Optical fourier transform scatterometry for LER and LWR metrology," Proc. SPIE **5752**, 192 (2005).
10. H. Gross, J. Richter, A. Rathfeld, and M. Bär, "Investigations on a robust profile model for the reconstruction of 2D periodic absorber lines in scatterometry," JEOS:RP **5**, 10053 (2010).
11. H. Gross, R. Model, M. Bar, M. Wurm, B. Bodermann, and A. Rathsfeld, "Mathematical modelling of indirect measurements in scatterometry," Measurement **39**(9), 782–794 (2006).
12. M. Wurm, F. Pilarski, and B. Bodermann, "A new flexible scatterometer for critical dimension metrology," Rev. Sci. Ins. **81**, 023701 (2010).
13. V. F. Paz, S. Peterhänsel, K. Frenner, and W. Osten, "Solving the inverse grating problem by white light interference fourier scatterometry," Light: Sci. Appl. **1**, e36 (2012).
14. M. Ryabko, S. Koptyaev, A. Shcherbakov, A. Lantsov, and S. Oh, "Method for optical inspection of nanoscale objects based upon analysis of their defocused images and features of its practical implementation," Opt. Express **21**, 24483–24489 (2013).
15. R. Attota, R. G. Dixson, J. A. Kramar, J. E. Potzick, A. E. Vladr, B. Bunday, E. Novak, and A. Rudack, "TSOM method for semiconductor metrology," Proc. SPIE **7971**, 79710T (2011).
16. L. Asinovski, D. Beaglehole, and M. T. Clarkson, "Imaging ellipsometry: quantitative analysis," Phys. Status Solidi (a) **205**(4), 764–771 (2008).
17. E. Halter, P. Montgomery, D. Montaner, R. Barillon, M. D. Nero, C. Galindo, and S. Georg, "Characterization of inhomogeneous colloidal layers using adapted coherence probe microscopy," Appl. Surf. Sci. **256**(21), 6144–6152 (2010).
18. D. G. Stavenga, H. L. Leertouwer, P. Pirih, and M. F. Wehling, "Imaging scatterometry of butterfly wing scales," Opt. Express **17**(1), 193–202 (2009).
19. B. K. Minhas, S. A. Coulombe, S. S. H. Naqvi, and J. R. McNeil, "Ellipsometric scatterometry for the metrology of sub-0.1- μm-linewidth structures," App. Opt. **37**(22), 5112–5115 (1998).
20. H. J. Patrick, T. A. Germer, Y. Ding, H. W. Ro, L. J. Richter, and C. L. Soles, "Scatterometry for in situ measurement of pattern reflow in nanoimprinted polymers," Appl. Phys. Lett. **93**, 233105 (2008).
21. O. El Gawhary, N. Kumar, S. F. Pereira, W. M. J. Coene, and H. P. Urbach, "Performance analysis of coherent optical scatterometry," App. Phys. B **105**, 775–781 (2011).
22. O. El Gawhary and S. Petra, "Method and apparatus for determining structure parameters of microstructures," European patent (WO/2012/126718) and US patent US 20120243004 A1 (2012).
23. N. Kumar, O. El Gawhary, S. Roy, S. F. Pereira, and H. P. Urbach, "Phase retrieval between overlapping orders in coherent fourier scatterometry using scanning," JEOS:RP **8**, 13048 (2013).
24. R. Silver, B. Barnes, A. Heckert, R. Attota, R. Dixson, and J. Jun, "Angle resolved optical metrology," Proc. SPIE **6922**, 69221M (2008).
25. N. Kumar, O. El Gawhary, S. Roy, V. G. Kutchoukov, S. F. Pereira, W. Coene, and H. P. Urbach, "Coherent Fourier scatterometry: tool for improved sensitivity in semiconductor metrology," Proc. SPIE **8324**, 83240Q (2012).
26. M. G. Moharam, and T. K. Gaylord, "Rigorous coupled-wave analysis of planar-grating diffraction," J. Opt. Soc. Am. **71**(7), 811–818 (1981).
27. M. G. Moharam, D. A. Pommet, E. B. Grann, and T. K. Gaylord, "Stable implementation of the rigorous coupled-wave analysis for surface-relief gratings: enhanced transmittance matrix approach," J. Opt. Soc. Am. A **12**(5), 1077–1086 (1995).
28. L. Li, "Use of fourier series in the analysis of discontinuous periodic structures," J. Opt. Soc. Am. A **13**(9), 1870–1876 (1996).
29. J. Hartmann, "Bemerkungen ueber den bau und die justierung von spektrographen," Zeitschrift fuer Instrumentenkunde **20**, 47–58 (1900).
30. W. H. Press, S. A. Teukolsky, W. T. Vetterling, and B. P. Flannery, *Numerical recipes in C (2nd ed.): the art of scientific computing* (Cambridge University Press, 1992).
31. W. H. Swann, "A survey of non-linear optimization techniques," FEBS Letters **2**, S39 (1969).

1. Introduction

The demand for faster, smaller, lighter and, at the same time, high-data density electronic devices sets stringent requirements for nanolithography, the science of writing small features into a photo-sensitive resist layer on top of a silicon wafer [1]. Already for the current 45 and 32 nm technology nodes, the uniformity of the line-width or critical dimension (CD) over the wafer as produced by lithographic scanners must be improved for an optimal yield and performance of the electronic components. In order to obtain the intended line shapes and sizes, a reliable in-line process control has to take place. This is achieved by printing special targets on the wafer, typically gratings, which are successively measured in order to adjust dose, exposure time, over-

#215012 - $15.00 USD Received 30 Jun 2014; revised 17 Aug 2014; accepted 19 Aug 2014; published 1 Oct 2014

lay/alignment and other relevant process parameters of the photo-lithographic machine [2, 3]. Currently, the metrology task of this process control is achieved by means of Incoherent Optical Scatterometry (IOS). In this technique, which is a very well established method for the inspection of periodic structures like gratings, an incoming beam is shone on the target and the part of the light which is scattered by it in reflection is measured in the far field. Given some *a priori* knowledge of the target, one can achieve high accuracies in the reconstruction of the shape of the grating. The advantage over other competing inspection techniques, such as imaging, Scanning Electron Microscopy (SEM) or Atomic Force Microscopy (AFM), is that IOS is a very fast technique which does not suffer from the Rayleigh diffraction limit, is easily integrable in a lithographic machine, and can cope with the high throughputs of today's scanners, in the order of 200 wafers per hour.

The way near field techniques utilize coupling of probe and sample cannot be utilized in production environment without decreasing the throughput. Rigorous far field techniques are in this sense a good alternative. However, such advantages also have a price since scatterometry falls into the category of inverse problems in electromagnetism, which are known for being severely ill-posed. Inverse problems occur in many other branches of science and technology as well. Ill-posedness in this context means that the successful reconstruction of grating parameters from the far field may not be possible, or may not be unique [4, 5]. This implies that even a very precise and accurate experimental far field signal does not always provide enough information content for reconstruction. It is the presence of some *a priori* information (as for example an approximate grating structure) that enormously reduces the impact of the ill-posedeness and makes scatterometry feasible in practice.

Many variations of the idea behind a scatterometer have emerged in the last decades [6]. Some of the most widely used configurations are single incidence angle reflectometry, 2-Θ scatterometry, spectroscopic ellipsometry, Fourier scatterometry, interferometric Fourier scatterometry,etc., [7–15] with a wide range of applications [16–20]. In an earlier paper, it has been predicted theoretically how, and under which conditions, CFS can be more sensitive than the classical IOS [21]. In this paper, we demonstrate the reconstruction of the parameters of a periodic grating using Coherent Fourier Scatterometry (CFS), which represents a step towards the further improvement of sensitivity of scatterometry in the sub-nanometer regime. Beside providing an accurate reconstruction of the grating's parameters, CFS also carries the strong potential of being used as subnanometer wafer alignment tool since the scattered signal is highly sensitive to the grating position as well. Last, but not least, CFS with focused spot is not limited to measuring periodic structures but can be applied to analysis of multilayer structures, material sciences, photonics industry, biosensing, detection of isolated structures and other forms of non-contact metrology.

2. Simulation and experimental considerations

2.1. Coherent Fourier scatterometry

In CFS, light from a coherent source is focused on periodic structures (typically gratings) on the wafer. The focused spot interacts with the grating and the far field is recorded [22]. In this way, the angular spectrum for all scattered waves is recorded at once for all incident plane waves within the focused spot. In the event of overlapping reflected orders in the lens pupil, there is interference between them and some phase information is also registered [23]. This is achieved by scanning the grating by means of a tightly focused beam, which allows resolving the phase information in practice. The number of scanning positions needed to resolve the phase depends upon the number of overlapping orders in the pupil of the focusing lens. Since the technique relies on the acquisition of the diffracted far field, methods to model the interaction between incident focused spot and the grating, which gives rise to such far field, must be implemented.

#215012 - $15.00 USD Received 30 Jun 2014; revised 17 Aug 2014; accepted 19 Aug 2014; published 1 Oct 2014

This task, called forward problem, is typically performed by means of a rigorous electromagnetic solver for a set of geometrical and physical parameters of the grating (Fig. 1.) under the predefined illumination conditions. In this way, the overall expected sensitivities of IOS and CFS have been computed and compared [24, 25].

2.2. Grating model and the illumination scheme

Let us consider an infinitely long one-dimensional grating with period Λ, which is invariant along the *y*-axis as shown in Fig. 1. The geometrical shape of the grating is defined by the parameters midCD (width of the grating lines at half of the total height), height and side wall angle (SWA). An additional metrology parameter, which we call bias, is also defined here. Bias is the measure of the grating displacement from its nominal position with respect to the illumination spot. Defined in this way, such parameter directly provides information on the alignment of the wafer which the grating has been printed on. The zero bias position can be chosen arbitrarily, and in our case, we choose it at the position where the optical axis of the microscope objective bisects the midCD (assuming a symmetrical grating profile). These parameters and the basic principle of data acquisition in CFS are shown in Fig. 1.

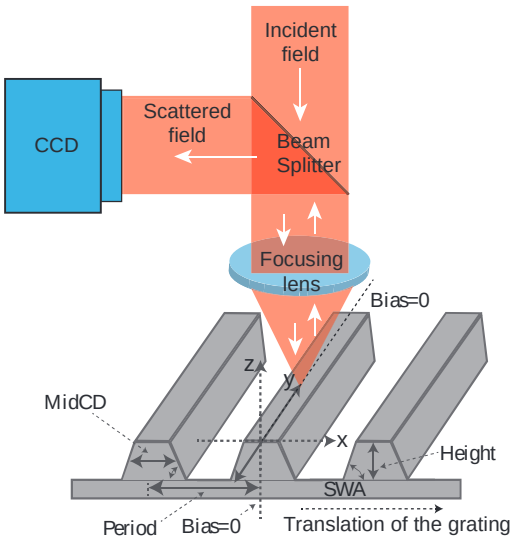

Fig. 1. Scheme of the CFS illumination, data acquisition system and the grating parameters.

A collimated light beam with a well-defined polarization state in the pupil of the lens is focussed on the grating and the scattered light is collected and collimated by the same lens, and detected by the CCD as illustrated in Fig. 1. Any change in the grating parameters results in a nonlinear change of the reflected far field. The total number of detected propagating diffracted orders depends on the wavelength (λ) of the incident light, the numerical aperture (*NA*) of the lens and the period (Λ) of the grating. The amount of overlap between the diffracted orders in the lens pupil is given by the overlap parameter *F*, defined as:

$$F = \frac{\lambda}{NA * \Lambda}. \tag{1}$$

#215012 - $15.00 USD Received 30 Jun 2014; revised 17 Aug 2014; accepted 19 Aug 2014; published 1 Oct 2014

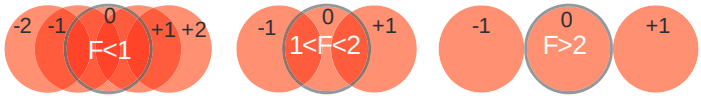

Fig. 2. Overlap between the diffracted orders depending upon the value of the overlap parameter F. The NA of the lens is marked with black circles.

As shown in Fig. 2, at the lens pupil, for $1 < F < 2$, there is an overlap between the 0^{th} and $\pm 1^{st}$ orders of the grating but no overlap between the -1^{st} and $+1^{st}$ order. For $F < 1$, however, there is an overlap between the higher diffracted orders, and for $F > 2$, there is no overlap between the orders.

2.3. *Grating fabrication*

The periodic structure used in the experiment is an etched silicon grating. To fabricate the grating, a cleaned silicon wafer was spin-coated with e-beam sensitive resist polymethyl methacrylate (PMMA). The grating pattern was written into the resist using electron beam lithography. After development of the resist, the grating pattern was etched into the silicon wafer using a reactive ion etching system (F1 Leybold Fluor ethna), with SF_6 gas as the etchant. The remaining resist layer was removed using dry oxygen plasma etch. The target parameters of grating fabrication are pitch=1300 nm, midCD=560 nm, height=115 nm, and SWA=90 degrees.

2.4. *Experimental setup*

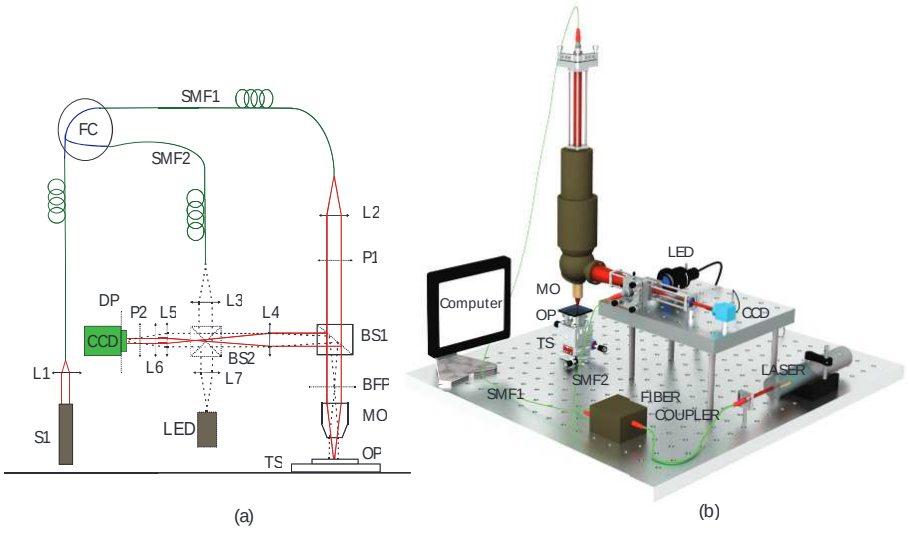

Fig. 3. Schematics of the experimental setup. (a) Ray diagram of the experimental scheme (S1: He-Ne laser, FC: Fiber coupler, SMF: Single mode fiber, LED: Light emitting diode, BS: Beam splitter, P: Polarizer, L: lens, DP: Detector plane, BFP: Back focal plane, OP: Object plane (grating), MO: Microscope objective, TS: Piezo-controlled translation stage). (b) 3D illustration of the laboratory setup.

Figure 3 represents the schematics of the coherent Fourier scatterometer. Light from a He-

#215012 - $15.00 USD Received 30 Jun 2014; revised 17 Aug 2014; accepted 19 Aug 2014; published 1 Oct 2014

Ne laser ($\lambda = 633$ nm) is coupled into a fiber which is then divided into two arms by a fiber coupler (FC). SMF1 and SMF2 are the illumination and the alignment arm, respectively. Light from SMF1 is collimated and polarized to provide a well-defined illumination of the sample through the microscope objective (MO). The incident light is selected to be either in TE or TM polarization configuration in the entrance pupil of the lens. The denomination TE(TM) here refers to the incident electric (magnetic) field in the pupil being oriented parallel to the grooves of the grating. The incident focused spot can be decomposed into plane waves with varying incident angles. The maximum angle of incidence is limited by the numerical aperture *NA* of the microscope objective MO. In the actual experiment, we used an objective with $NA = 0.4$. Each allowed incident angle contributes to the reflected diffraction orders which propagate back through the MO to the CCD. The diameter of the collimated reflected beam is reduced by a telescopic system, which images the back focal plane (BFP) of the MO onto the CCD with a demagnification of 2.5X to fit into the CCD area (1600 $\times$ 1200 pixels, size of 3.75 μm $\times$ 3.75 μm per pixel). In the Fourier or back focal plane (BFP) there is an interference between the reflected orders for the chosen *F* number ($1 < F < 2$, see Fig. 2). The polarizer P2 in the experimental setup can be used to detect a selected polarization at the CCD. SMF2 is used to align the telescopic system. The red LED light source is only used to image the grating on the CCD camera for alignment purposes during the preparation of the experiment. Components BS2 and L6 are removed during data acquisition. The solid red line in the ray diagram of Fig. 3(a) is the data acquisition path and the black dotted paths are used only for alignment and imaging. In the setup, the telescopic lenses L4 and L5 are used for data acquisition; and lens L6, beam splitter BS2, and lenses L4 and L5 are used for alignment and imaging.

3. Results and discussion

3.1. Diffracted far field intensity maps

Along with the acquisition of experimental data, scatterometry also requires an accurate modelling of the interaction between field and sample. We used the rigorous coupled wave analysis (RCWA) as the rigorous solver to compute the field diffracted by the grating [26–28]. In order to make the simulations as faithful as possible, the measured amplitude and phase distribution of the incident field is included in the RCWA simulations as well. The amplitude for the incoming beam is practically uniform (measured by CCD and SHS) and the phase in the entrance pupil of the lens is measured with a Shack-Hartmann wavefront sensor (SHS) [29]. In Figs. 4(a) and (a′) the measured wavefronts for TE and TM polarizations on the lens pupil expressed in units of wavelength of the incident light are shown. The far field intensity maps for a fixed bias shown in Fig. 4 are the simulated and measured data obtained for a silicon etched grating having an overlap parameter $F = 1.2$ (see Fig. 2) for $NA = 0.4$ at the wavelength of 633 nm. Far field intensity maps b, c and d (b′, c′ and d′) represent respectively the simulation, experiment and the difference between them for best matched fit for TE (TM) incident light on the lens pupil and mixed output polarization (i.e., no polarizer is used in the detection path). In the simulations, the measured wavefront with a Shack-Hartmann sensor (SHS) is used to compute the diffracted far field intensity maps. The camera has been tested for noise by measurements, where each far field intensity map is averaged over 10 frames. Also, we consider the measured noise of the CCD camera as normally distributed with standard deviation given by measured uncertainties of $\sigma = 1 \times 10^{-3}$. While the energy in the diffracted order depends upon the grating parameters, the extent of overlap between the diffracted orders in the far field is given by the overlap parameter *F*.

It is to be noted that the sensitivity of grating parameters (change of the far field maps) is different for TE and TM incident polarized light. In CFS,in the overlap region there is interference between the grating orders and the phase change due to the shift of the grating can be related to

#215012 - $15.00 USD Received 30 Jun 2014; revised 17 Aug 2014; accepted 19 Aug 2014; published 1 Oct 2014

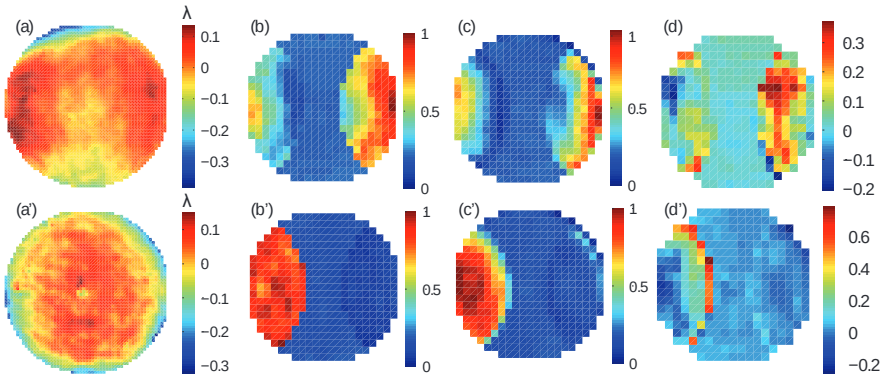

Fig. 4. Simulated and experimental far field intensity maps for a fixed bias value and the difference between the simulation and experiments. Wavefront for TE (a) and TM (a′) incident polarizations on the lens pupil. Far field intensity maps b, c and d (b′, c′ and d′) represent the simulation, experiment and the difference between them for best matched fit for TE (TM) incident light on the lens pupil and mixed output polarization. The diameter of the pupil in a and a′ is 8 mm.

the change in far field intensity maps for different bias values. The amount of phase shift in the non-zero order due to translation distance δx is given by

$$\delta\phi = \frac{2\pi m \delta x}{\Lambda}, \tag{2}$$

where m is the order number of the reflected order.

3.2. *Bias correlation*

Wafer positioning is an important issue in the industrial manufacturing process. Being a phase sensitive technique CFS introduces a change in the far fields with scanning position on the grating. In the experiments, far field intensity maps for consecutive scan positions (bias) of 20 nm difference were recorded over the length of several periods of the grating. The ability to distinguish between the intensity maps defines the sensitivity to bias of the present experimental setup. The degree of correlation 'r' (correlation coefficient) is used as a measure to distinguish experimental images:

$$r = \frac{\sum_x \sum_y \left[I_{xy}^{ref} - \bar{I}^{ref} \right] (I_{xy} - \bar{I})}{\sqrt{\sum_x \sum_y \left[I_{xy}^{ref} - \bar{I}^{ref} \right]^2 \sum_x \sum_y (I_{xy} - \bar{I})^2}}. \tag{3}$$

Here, I^{ref} and I (x and y are pixels) are the far field intensities corresponding to the starting bias position called reference and the other scanning positions. $\bar{I}^{ref}$ and $\bar{I}$ are the corresponding mean values for I^{ref} and I. The correlation coefficient $'r'$ has values between -1 to 1. When the intensity maps are completely correlated, r=1, while r=0 implies no correlation and there is complete anti correlation between the intensity maps for r=-1. In Fig. 5, value of correlation coefficient derived from the experimental far field intensity maps is shown for bias values ranging from 0 to 1.3 μm (one period of the grating). Figure. 5(a) plots the correlation coefficients

#215012 - $15.00 USD Received 30 Jun 2014; revised 17 Aug 2014; accepted 19 Aug 2014; published 1 Oct 2014

for scanning positions within one period of the grating. Figure 5(b) is the color label adjusted plot to highlight the sensitivity of bias.

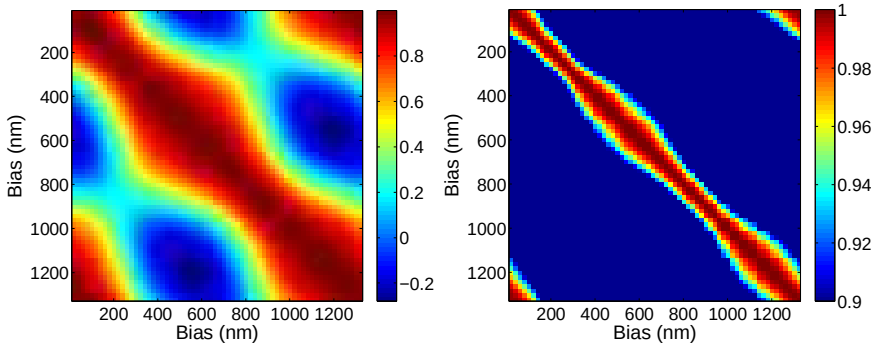

Fig. 5. Degree of correlation between experimental far field intensity maps. (a) Correlation coefficients for positions separated by 20 nm for bias values within one period of the grating (b) The same as a), but only showing the range points where $0.9 < r < 1$.

From the above analysis of the experimental data, it is evident that CFS is highly sensitive to grating position. However, for a symmetric grating, absolute positions may also be determined regarding the symmetric position within a period of the grating (like the middle of the midCD, for which the far fields are also symmetric). In CFS, nm and sub-nm positioning within a single period of the grating can be reached in wafer alignment in semiconductor industry, also shown in the reconstructed values (see Table 1 further in the text). This feature can also be used in other application as in imprint technology.

3.3. Model based optimization

Solving the inverse problem of grating reconstruction with CFS amounts to the determination of the values of the grating parameters for which the computed scattered far field maps fit best the experimentally measured images. The grating parameters defined in Fig. 1 lie in certain intervals obtained from *a priori* information and from the design specification of the grating. Starting from the nominal values of the grating parameters, the deviation between the experimental and simulated images are minimized, using a least square function (merit function) by varying the grating parameters. The diffracted far field of the grating depends on the known experimental conditions and the unknown grating parameters. Let **a** denote the grating parameters and $I_{i,j}^{(m)}$ and $I_{i,j}^{(s)}$ the measured and simulated far field intensities at the i^{th} CCD pixel and j^{th} scan position. The merit function to be minimized is the difference between the simulated and experimental far field intensities summed over all the incident angles in the entrance pupil and pixels over the detector. The merit function is thus given by

$$f(\mathbf{a}) = \sum_{j=1}^{S} \frac{1}{N} \sum_{i=1}^{N} \left[I_{i,j}^{(m)}(\mathbf{a}) - I_{i,j}^{(s)}(\mathbf{a}) \right]^2, \tag{4}$$

where S is the total number of scan positions and N is the total number of pixels at the detector for a single far field intensity map. We use a gradient-based non-linear optimization method to minimize the merit function defined in Eqn. 4 [30]. It can be minimized using library search or real time optimization methods [31]. In library search, several sets of far fields for approximate

#215012 - $15.00 USD Received 30 Jun 2014; revised 17 Aug 2014; accepted 19 Aug 2014; published 1 Oct 2014

grating parameters lying in the defined intervals are computed. Subsequently, the set of grating parameters for the minimal value of the merit function (Eqn. 4) is selected as the desired value of the grating parameters. It is to be noted that the optimization algorithm finds only the local minima. Here we use a gradient based non-linear least squares real time optimization method implemented in MATLAB. As *a priori* information in optimization, the target parameters of grating fabrication (listed in the text in section 2.3) are used. Figure 6 shows a set of simulated and experimental far fields for bias values lying within a single period of the grating obtained with TE incident light on the lens pupil and no polarizer at the detector for the grating parameters corresponding to the minimized merit function. Consecutive far fields (numbered 1 to 12) correspond to consecutive grating positions for a bias difference of 100 nm.

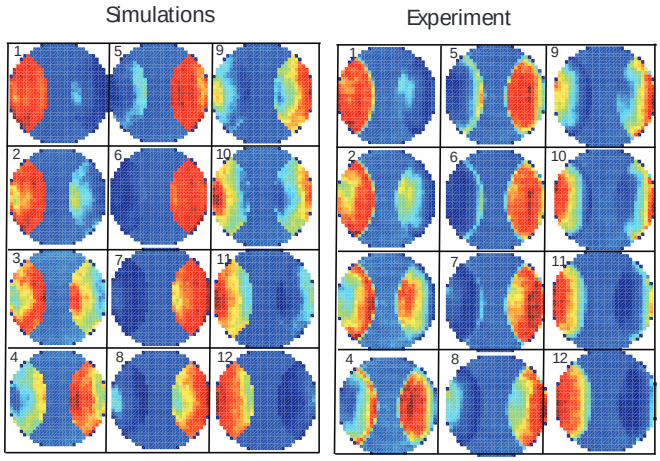

Fig. 6. Simulated and experimental far field for TE incident polarization on the lens pupil and no polarizer at the detector for the grating parameters corresponding to the minimized merit function. The bias position is changed by 100 nm between consecutive far fields (numbered 1 to 12).

3.4. Parameters reconstruction and discussion

The reconstructed grating parameters are listed in Table 1 (for all the grating parameters including bias are fitted together in the optimization). The far field intensities used for the reconstruction algorithm is a set of data such as shown in Fig. 6 but the incident fields are TE and TM polarized and no polarizer at the detector side. To verify the results, the grating was also measured by SEM and AFM. The SEM measurement was performed with a Hitachi S 400 scanning electron microscope at 4 kV with a magnification of 35000. The uncertainties of the CFS and SEM were determined from repeated evaluations. In the case of the SEM, the uncertainty of the measured midCD was determined from measurements at different parts of the image (so the uncertainties are partly caused by line edge roughness). The bright edges of the grating lines were the main cause of the uncertainties. This edge is clearly seen in Fig. 7(a). The uncertainty of the height measurement with the AFM can be estimated using the histogram of Fig. 7(c). The uncertainties are in the “few nanometers” range for all techniques. A low-uncertainty measurement with AFM (without the 3D option) and SEM (without cutting the sample) is only possible for height and CD, respectively. The $3-\sigma$ uncertainty in the grating parameters reconstruction by means of CFS is lower compared to that obtained through SEM and AFM measurements. We notice higher relative uncertainties in SWA reconstruction as compared to height and midCD uncertainties, which are also reported by others [13].

#215012 - $15.00 USD Received 30 Jun 2014; revised 17 Aug 2014; accepted 19 Aug 2014; published 1 Oct 2014

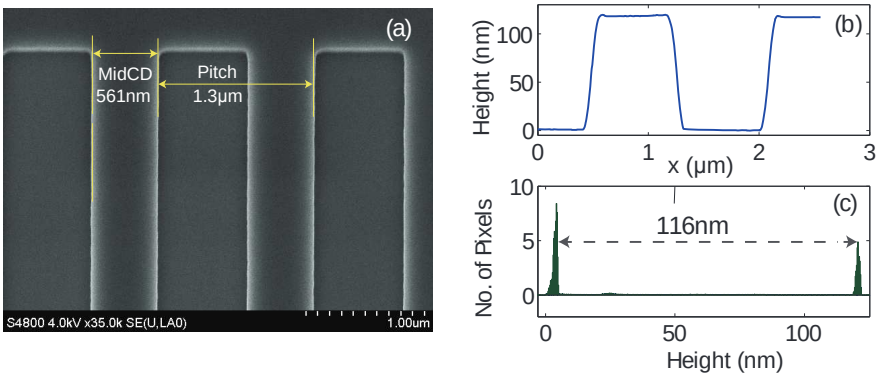

Fig. 7. (a) Top view of the SEM image. (b) AFM cross section in the direction perpendicular to the grating lines. (c) Histogram of heights for each pixel of the AFM measurement.

Table 1. Comparative measurements of the grating parameters using different techniques.

Parameters	CFS	SEM	AFM
MidCD (nm)	563±2	562±4	–
Height (nm)	116±1	–	116±3
SWA(°)	89±3	–	–
Bias (nm)	1190±1	–	–

The results are compiled in table 1 for $NA = 0.4$ and at $\lambda = 633$ nm. Interestingly, the lateral position of the grating can be retrieved with an accuracy at 1 nm level, which is an impressive accuracy, considered the numerical aperture of the system and the wavelength used. Actually, an accurate retrieval of the alignment parameter bias is a fundamental pre-requisite for CFS to work. In fact, no reconstruction of the grating parameters would be possible without first determining the relative position between incident spot and grating. We have also performed simulations studies, in order investigate to which level of accuracy the alignment can be obtained through CFS measurements. We have found that, by using an incident field with $\lambda = 250$ nm, $NA = 0.95$ and a grating with pitch 200 nm (all these values are very well representative of a current state-of-the art industrial IOS) positioning accuracy at 10 pm level is attainable. Simulation studies show that at such high NA and shorter wavelength the uncertainty in reconstruction of the grating parameters can be further decreased as well. All these benefits can be attributed to the phase sensitive signal, as for $F < 2$ CFS can be seen as a common path interferometer.

4. Conclusions

Grating reconstruction with coherent Fourier scatterometry (CFS) has been demonstrated. The tool is capable of illuminating and measuring the response of the sample simultaneously over a broad range of incident and reflected angles. The measurement for all radial and azimuthal angles can be performed within one second. Due to the coherent illumination, the measuring spot can be focused to a size smaller than one micron. Compared to incoherent scatterometry the advantage of coherent Fourier scatterometry is that the measured response in the pupil plane includes interference patterns caused by overlapping orders. The interference changes when the spot is scanned perpendicularly to the grooves of the grating, and consequently the phase information contained in the overlapping orders can be determined accurately. The capabilities

#215012 - $15.00 USD Received 30 Jun 2014; revised 17 Aug 2014; accepted 19 Aug 2014; published 1 Oct 2014

of the tool were demonstrated by reconstructing the parameters of grating with 1300 nm pitch using a wavelength of λ= 633 nm and an objective lens of $NA = 0.4$. The reconstruction was performed by non-linear least squares gradient fit of the grating parameters to minimize the difference between the measured and rigorously computed pupil images. The sensitivity of coherent Fourier scatterometry was found to be comparable with the applied reference metrologies (SEM and AFM). In addition, simulation studies show that positioning accuracy of the order of 10 picometer with $NA = 0.95$ and λ in the UV can be achieved. Finally, it is worth mentioning that accurate nano-positioning in combination with the reconstruction shape parameters of the grating can be done in a single tool which is not possible in conventional optical scatterometry.

Acknowledgments

The authors acknowledge Mark Van Kraaij from ASML, Veldhoven. Peter Petrik is grateful for the EMRP IND17 joint research project on scatterometry for financial support. The EMRP is jointly funded by the EMRP participating countries within EURAMET and the European Union.

#215012 - $15.00 USD Received 30 Jun 2014; revised 17 Aug 2014; accepted 19 Aug 2014; published 1 Oct 2014